Progress in Additive Manufacturing (2026) 11:6645–6660
https://doi.org/10.1007/s40964-026-01659-y

RESEARCH

Process parameter optimization for enhanced mechanical performance in PBF-LB/M of AISI 316L using constant energy density

Beatriz Achiaga[1] · Blanca Castaño[1] · Daniel Gomez-Lendinez[2] · Rafael Barea[2] · Lorenzo Pedrolli[1] · Alejandro Lopez[1]

Received: 23 October 2025 / Accepted: 23 March 2026 / Published online: 29 May 2026

Abstract
Laser powder bed fusion (PBF-LB/M) is an additive manufacturing technology (AM) for producing metal components with complex geometries. The mechanical properties of these components play an important role in their performance and functionality. This work has found the process parameters to achieve the optimal properties of AISI 316L stainless steel using SamyLabs Alba 300 system. A Design of Experiments approach was employed under a constant volumetric energy density constraint to identify optimal parameter combinations (laser power, laser frequency, scanning speed and hatching distance). Tensile testing and metallographic analysis show that even at fixed energy input, the material's properties were still affected by the process parameters. Specifically, higher laser frequencies and reduced scanning speeds, combined with increased hatching distances, led to improved mechanical performance with a significant positive impact on tensile strength and hardness of the manufactured parts. The results demonstrate that laser frequency plays a critical role in melt pool dynamics. Optimal settings derived from this study provide a reliable guideline for enhancing part quality in PBF-LB/M processes and can be extrapolated to similar AM systems.

Keywords PBF-LB/M · AISI 316L stainless steel · Process parameter optimization · Volumetric energy density (VED) · Mechanical properties · Keyhole Number

1 Introduction

Metal Additive Manufacturing, specifically PBF-LB/M—also known as Selective Laser Melting (SLM)—technology, has been increasingly adopted across various industries due to its versatility and advantages over conventional manufacturing processes [1]. Among the many benefits of PBF-LB/M, significant cost savings, reduced production times, and the ability to fabricate intricate geometries while offering customization options stand out as essential [2].

With rapid advancements in PBF-LB/M technologies expected over the next decade, its growing relevance in the manufacturing landscape is becoming increasingly evident. PBF-LB/M is making a significant impact across numerous sectors, including transportation, medicine, sports, and electronics. The quality and performance produced using PBF-LB/M technologies continue to influence and enhance development in these industries [3].

PBF-LB/M works by systematically melting successive layers of metal powder using a high-power laser, precisely guided by predefined geometrical specifications and finely tuned parameters managed by specialized software tools [4]. As an additive manufacturing method, PBF-LB/M facilitates the creation of lightweight components, delivering a considerable advantage over traditionally manufactured pieces.

✉ Beatriz Achiaga
beatriz.achiaga@deusto.es

✉ Lorenzo Pedrolli
l.pedrolli@deusto.es

Blanca Castaño
blanca.castano@opendeusto.es

Daniel Gomez-Lendinez
dgomezle@nebrija.es

Rafael Barea
rbarea@nebrija.es

Alejandro Lopez
alejandro.lopez@deusto.es

1 Faculty of Engineering, University of Deusto, Bilbao, Spain

2 Escuela Politécnica Superior, Nebrija University, Madrid, Spain

Recognizing the inherent limitations of PBF-LB/M techniques is essential, as they face challenges such as suboptimal surface finish, dimensional accuracy, and material properties, including microstructure and mechanical performance [5]. These limitations have hindered the widespread adoption of PBF-LB/M across various industrial sectors. Addressing these limitations requires a deeper understanding of the complex relationship between processing parameters and their impact on the final product's quality [6, 7]. Furthermore, it is crucial to acknowledge that many of these drawbacks (and their corresponding solutions) are often specific to the particular 3D printing system employed in the process [8, 9].

In the context of lightweight materials suitable for PBF-LB/M processing, titanium and aluminum alloys have emerged as the most widely used options, while stainless steel—particularly AISI 316L—is also gaining increasing relevance. Common lightweight candidates include commercially pure titanium (CP-Ti), Ti–6AI–4V (Ti64) as aluminum–silicon (Al–Si) alloys, with AlSi10Mg standing out due to its similarity to the A360 alloy [7, 10–13]. Extensive research has developed into various aspects, covering from the characterization of initial powders to the exploration of potential applications of these lightweight alloys, in some cases considering the fabrication of lattice structures [10, 13].

Collectively, existing research underscores the substantial influence of printing parameters and equipment selection on microstructure and the final properties of manufactured components [1, 6]. While considerable research has discussed the effects of printing parameters on materials such as titanium and aluminum [14, 15], a noticeable research gap exists regarding the influence of these parameters on stainless steel, particularly on 316L. Furthermore, variations in equipment and environmental conditions can significantly impact material properties [16]

This study aims to clarify the individual influence of key PBF-LB/M processing parameters under constant volumetric energy density, a condition rarely explored for 316L, thereby providing new insight into how parameter sensitivity governs melt-pool stability and final part performance. The study investigates the combinations of process parameters that enable the fabrication of dense specimens with optimal mechanical properties using the printer Samylabs Alba300. The sensitivity of the process to each parameter is also analyzed, identifying a physical reason for their effect on the final mechanical properties. The findings are transferable to similar PBF-LB/M equipment and contribute to the development of a more generalized methodology to determine optimal processing conditions in metal additive manufacturing.

2 Methods and development

In laser-material processing, specifically within Laser Powder Bed Fusion (LPBF), Volumetric Energy Density (VED) is traditionally established as a fundamental metric to quantify the energy delivered per unit volume of the powder bed. It is defined by the relationship between laser power (P), scanning speed (v), hatching distance (h), and layer thickness (t). For this study, to accurately reflect the nature of laser emission modulated using PWM, the standard formulation has been refined by substituting continuous power with the product of laser power and cycle time (P × c). This adaptation enables a more precise characterization of the effective energy input during pulsed interactions, where the temporal distribution of energy significantly influences the part's thermal history [17].

The primary strength of VED lies in its role as a standardised design guideline for initial parameter selection during the design of experiments (DoE) [18]. It serves as a comprehensive index for evaluating the relative density of components, with studies confirming that increasing VED generally improves material consolidation and reduces macroscopic "lack of fusion" (LoF) defects. Furthermore, VED is a reliable predictor of top-surface quality; higher energy inputs promote more effective melting of powder particles, resulting in more stable, continuous laser tracks and diminished surface roughness [19, 20].

Despite its widespread application, VED remains a purely thermodynamic quantity that fails to capture the complex kinetics of melt pool physics, such as Marangoni convection, hydrodynamic instabilities, and vapor recoil p ressure [21]. Research demonstrates that maintaining a constant VED does not guarantee consistent workpiece characteristics, as varying individual laser parameters can produce significant differences in roughness, density, and microhardness [22]. Moreover, VED is incapable of accurately predicting the critical transition between conduction and keyhole melting modes, where excessive energy input causes metal vaporisation and the formation of deep melt pools that trap gas bubbles and increase porosity [21].

The efficacy of VED is further constrained by its exclusion of intrinsic material properties and scale-dependent factors. For instance, the particle size distribution (PSD) of the powder bed significantly influences packing density and surface finish independently of the applied energy [20]. Furthermore, VED does not account for the impact of scanning strategies or component size; optimal parameters for small specimens often fail to achieve the same relative density in larger parts due to thermal gradient accumulation, necessitating advanced scanning patterns or intermediate layers to mitigate columnar porosity [23]. Consequently, VED serves only as a broad guideline and cannot anticipate the specific

Table 1 Powder specifications of 316L Steel provided by the manufacturer

Specification	Alloy, iron-based
Chemical composition (Weight percentage)	Fe (balance); Cr (18); Ni (12); Mo (2); C (<0,03); Others (<1)
Nominal particle size range	40 ± 15 µm
Volume percentile values	D10: 19 µm D50: 30 µm D90: 46 µm
Manufacture	Inert gas atomized (Argon)
Morphology	Spherical
Apparent density	<4 g/cm^3
Solidus	1390 ± 10 °C (2534 ± 18°F)
Liquidus	1448 ± 10 °C (2638 ± 18°F)
Process	PBF-LB/M

defect morphology and distribution that ultimately govern a component's fatigue behaviour [19].

Laser power, laser frequency, scanning speed, hatching distance, and layer height are among the most influential parameters affecting the final material properties [24, 25]. The powder material has a specific energy requirement to ensure complete melting and, in principle, obtain properties as close as possible to those of the bulk material [26]. The parameters selected must be combined to generate the specified energy input and are common in PBF-LB/M equipment [26, 27].

The process parameters were selected within the operational limits specified by the machine's manufacturer. The total energy input was calculated as a function of the process parameters, following the formulation by Greco et.al. [22] with similar approaches reported in other studies [20, 21, 23, 28].

$$E = \frac{P \cdot c}{V \cdot DL \cdot hc} \tag{1}$$

where P is the laser power, c is the cycle time, V the scanning velocity, DL the hatching distance and hc is the layer height.

2.1 Material and equipment

The material used in this study was Oerlikon MetcoADD 316L-A, stainless steel powder, whose characteristics, as declared by the manufacturer are reported in Table 1. This alloy is widely used in additive manufacturing due to its high corrosion resistance, good mechanical strength, and is excellent processability [29].

Figure 1a, b show Scanning Electron Microscopy (SEM) images of the powder morphology. The particles are mostly spherical, within the size distribution specified by the manufacturer (Table 1), and some particles exhibit the so-called "splat cap" geometry which is typical of atomized powders.

The manufacturing process was carried out using Alba 300 printer (SamyLabs). The build envelope of the printer has a diameter of 160 mm and a height of 200 mm. This PBF-LB/M system is equipped with a continuous-wave (CW) fiber laser operating at 1080 nm (Raycus RFL-300), with a maximum power of 300 W and a spot size of 70 µm. This type of laser always operates at the same power level (300W), but can be modulated to a lower nominal power using a pulse-width modulation (PWM) at frequencies up to 41 kHz, resulting in an energy delivery in discrete bursts although the laser source remains CW.

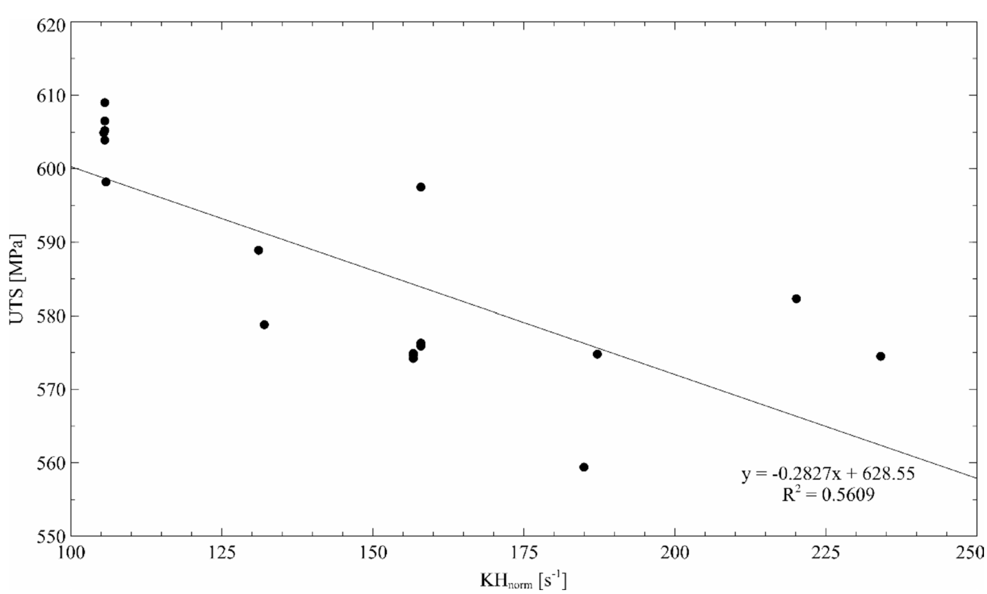

Fig. 1 SEM for the AISI 316L powder – × 100 and × 250 magnification

Table 2 Limits of the Process parameters modified

Process parameter	Upper limit	Lower limit
P (Laser power)	300 W (100%)	180 W (60%)
DL (hatching distance)	0.16 mm	0.08 mm
V (Scanning speed)	1400 mm/s	600 mm/s
F (Laser frequency)	10 kHz	45 kHz

2.2 Design of experiments

To determine the optimal printing parameters, it is essential to manufacture components under varying processing conditions and subsequently evaluate their performance. This study uses a Design of Experiments (DOE) approach to optimize the process, significantly reducing the number of experimental trials while improving time and cost efficiency [30, 31]. Moreover, this approach establishes statistically robust and reproducible results. DOE techniques have been widely applied in the analysis of PBF-LB/M [32, 33]. By systematic variation of one or more input variables, such as laser power, scanning speed or hatching distance, it is possible to evaluate their individual and combined effects on the resulting materials. In this case, one parameter is varied while the other is held as the unknown.

The primary objective of this experiment is to identify the optimal combination of process parameters that maximizes the mechanical properties of Stainless Steel 316L, while minimizing the number of experimental runs. To fabricate samples under different printing conditions, the volumetric energy density was calculated using Eq. (1) and maintained constant at 54.54 J/mm^3. The selected energy density was empirically determined by the machine manufacturer in a joint collaboration with the powder manufacturer. The value is consistent with the ones reported for PBF-LB/M systems of comparable design [34]. Although volumetric energy density does not fully capture the complexity of melt pool dynamics in laser powder bed fusion (PBF-LB/M), maintaining it constant provides a practical framework for isolating the influence of individual process parameters. This approach ensures sufficient particle cohesion and helps prevent defects such as lack of fusion or material degradation [35, 36].

On this basis, the manufacturer-recommended process parameters corresponding to this energy density were adopted as a baseline for the present study; however, the objective is to establish a more rigorously optimized parameter set through systematic variation around this baseline. The baseline conditions consist of a laser power setting of 80% (corresponding to 240W, controlled via Pulse Width Modulation, PWM), a scanning speed of 800 mm/s, a hatch distance of 0.1 mm, and a laser frequency of 37 k Hz.

The allowable ranges for each parameter, determined by extending the limits around the baseline values, are listed in Table 2. The process takes place in a controlled argon atmosphere with an oxygen concentration below 0.5%.

Table 3 Process parameters set, with a constant energy density

Nº	Power P (%)	Hatching distance DL (mm)	Scanning speed V (mm/s)	Frequency F (kHz)
1	83	0.115	800	37
2	70	0.098	800	37
3	60	0.082	800	37
4	100	0.138	800	37
5	83	0.110	833	37
6	70	0.110	717	37
7	60	0.110	600	37
8	100	0.110	1000	37
9	80	0.080	1375	37
10	80	0.110	1000	37
11	80	0.140	785	37
12	80	0.160	688	37
1.1	83	0.115	800	10
1.2	83	0.115	800	45
5.1	83	0.110	833	10
5.2	83	0.110	833	45
10.1	80	0.110	1000	10
10.2	80	0.110	1000	45

Four levels were generated for the first three parameters (P, dl, V), resulting in 12 parameter combinations. Each combination was adjusted to comply with the constraint of constant total energy input defined by Eq. (1). These combinations are reported in Table 3 (samples 1–12), while the laser frequency was maintained constant at 37 kHz, limiting the number of permutations.

Laser frequency is known to influence the volume of powder affected by the laser beam and is expected to have a strong impact on both the resolution and mechanical properties of the printed part. Since laser frequency is not included in Eq. 1, it was investigated separately using a reduced set of permutations of three cases (samples 1, 5, and 10), each tested at three frequency levels (10–37–45 kHz), also reported in Table 3.

A total of 18 parameter combinations were tested, with 5 specimens fabricated for each condition resulting in 90 printed samples. Tensile testing was performed according to the ASTM E8/E8M standard using a Metrotec MTE-300 universal testing machine. The microstructure was analyzed after etching polished cross-sections with Aqua Regia, allowing the identification of metallurgical phases (austenite, ferrite, pearlite) and eventual porosity.

All specimens were modeled as STL geometries and introduced into the printer's software definition. Each sample was labelled with an identification number engraved on the clamping ends. The layer thickness was defined to be 0.05 mm, and support structures were generated exclusively at the base of the specimens. The infill consisted of

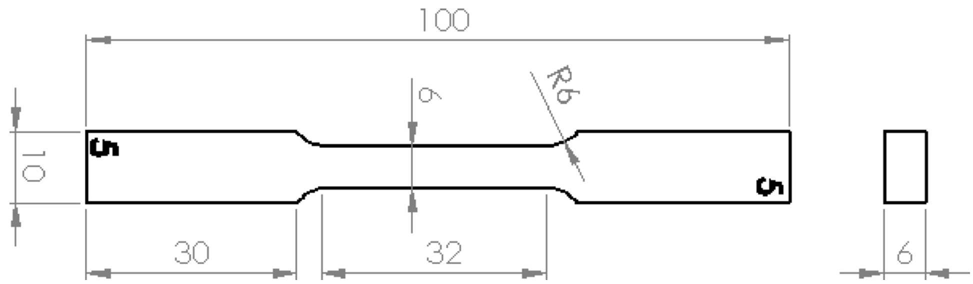

Fig. 2 Schematic illustration of the ASTM E8/E8M tensile specimens manufactured in this work

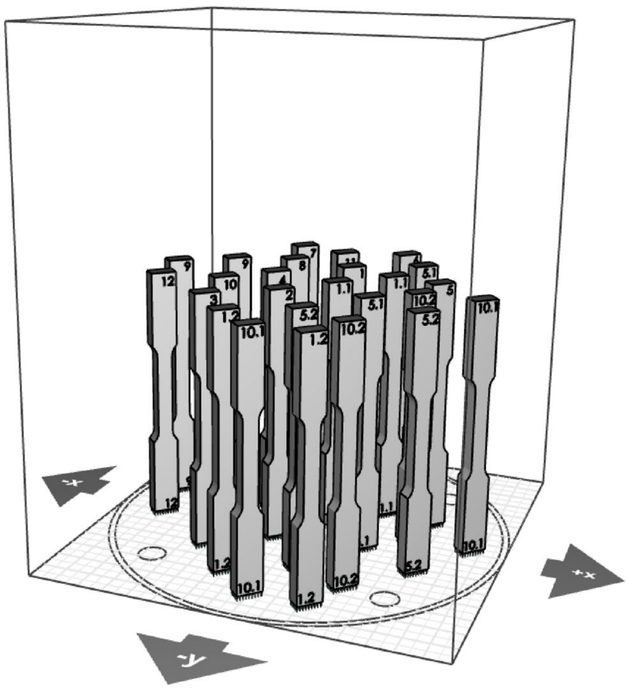

Fig. 3 Printing orientation of the samples: they are aligned longitudinally along Z, while XY is the printing plane

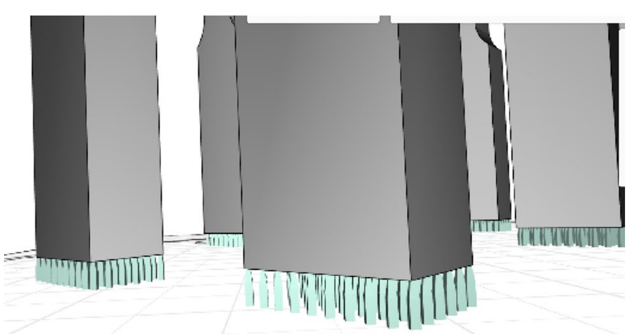

Fig. 4 Supports for manufacturing the samples

Table 4 Supports characteristics

Relative support density	0.3
Distance between supports	0.9 mm
Body diameter	0.8 mm
Contact tip diameter	0.4 mm
Total support height	7 mm

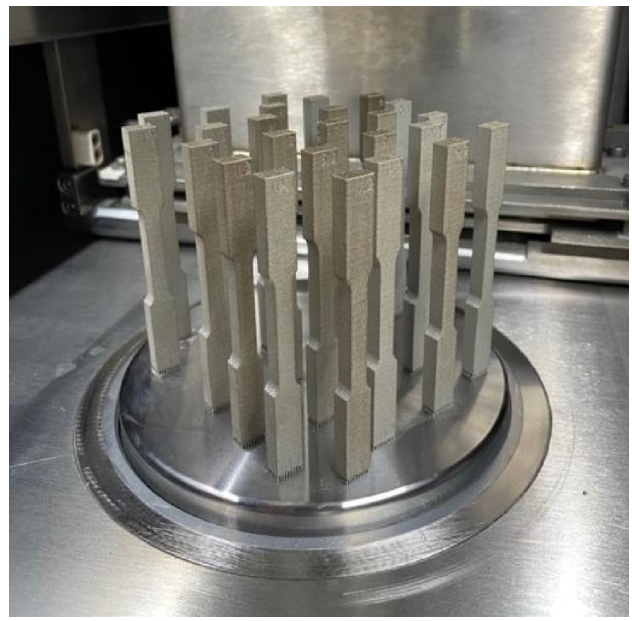

Fig. 5 Manufacturing of the Test samples

bidirectional scanning lines, rotated by 67º between layers. All specimens were printed in a vertical orientation (perpendicular to the build plate) with a support structure (Fig. 2). The resulting print bed layout is shown in Figs. 3 and 4, with the support's characteristics reported in Table 4. Figure 5 shows one of the complete prints.

3 Results and discussion

3.1 Mechanical properties

The mechanical properties of the samples were evaluated through uniaxial tensile testing using a Metrotec MTE-300, following the ASTM E8/E8M standard. Each parameter combination was tested on five printed specimens, and the result of a representative test is shown in Fig. 6. The average mechanical properties obtained for each condition are summarized in Table 5.

Table 5 presents the average mechanical properties obtained for each tested parameter combination, including yield strength, ultimate tensile strength (UTS), and Young's

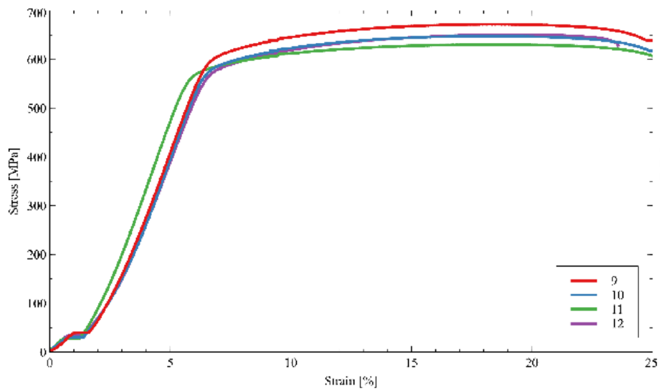

(a)

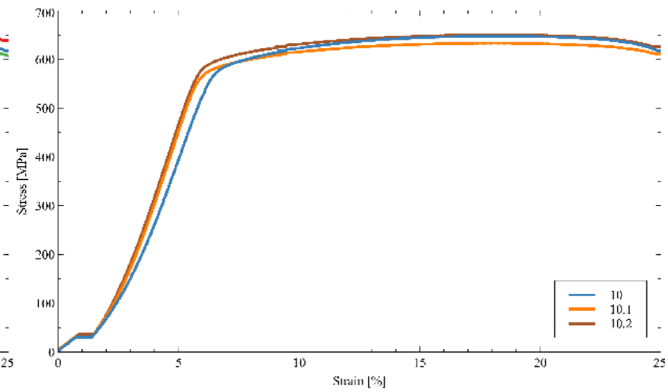

(b)

Fig. 6 **a** Stress–strain curve for test conditions 9,10,11 and 12.: A slight step observed in the initial elastic region is attributed to grip slip or machine signal noise, and does not affect the interpretation of the mechanical response **b** Stress–strain curve for test conditions 10.1, 10.2 and 10, where the only parameter varying is the laser frequency. Note: A slight step observed in the initial elastic region is a common occurrence attributed to grip slip or machine signal noise, and does not affect the interpretation of the mechanical response

Table 5 Resulting mechanical properties

Nº	Yield strength (MPa)	Ultimate tensile stress (UTS) (MPa)	Young's Modulus (GPa)
1	482±113	574±23	89±16
2	452±51	574±5	72±13
3	453±92	574±5	111±47
4	455±89	588±6	166±19
5	438±84	597±19	90±10
6	411±30	559±3	74±9
7	431±22	582±3	131±55
8	432±36	578±6	166±90
9	442±38	605±9	105±48
10	413±38	603±5	115±13
11	454±40	598±5	151±26
12	485±23	604±16	198±78
1.1	411±44	574±5	98±13
1.2	383±21	574±7	88±9
5.1	461±91	576±8	79±38
5.2	406±21	575±1	86±10
10.1	448±38	606±3	89±4
10.2	457±44	609±5	92±7

modulus. For the first twelve samples (conditions 1 to 12), corresponding to the baseline and energy-constrained permutations, Young's modulus exhibited moderate variability, with a standard deviation of approximately 5% (in the first eight conditions). In contrast, UTS and yield strength showed lower variation among replicates, indicating a more stable response to the applied processing conditions.

Additional tests conducted on selected conditions (samples 1.1, 1.2, 5.1, 5.2, 10.1, and 10.2), corresponding to different laser frequencies, also yielded consistent mechanical performance, with minor deviations from the baseline cases. These results suggest that while Young's modulus is somewhat sensitive to microstructural changes induced by process variations, strength-related properties remain more robust across tested conditions.

Within these results, the Young's modulus exhibits a substantially larger standard deviation than the other tensile properties measured in this study. Such scatter is consistent with previous work on PBF-LB/M 316L, where stiffness is highly sensitive to porosity and local defect structure [36]. Weaver et al. showed that, for PBF-LB/M 316L with 0–4% porosity, the average modulus from indentation and tensile tests agreed well, but the test-to-test scatter increased considerably in the presence of porosity, which they attributed to variations in the amount of porosity within the interaction volume under the indenter [36]. This result highlights that even small changes in local pore content can strongly affect the measured elastic response.

At the component scale, Jost et al. quantified porosity populations in PBF-LB/M 316L tensile specimens and demonstrated that global tensile properties, including apparent stiffness, are strongly controlled by defect characteristics such as pore size, morphology, and location [37]. Their defect–property analysis underlines that differences in internal defect populations between nominally identical samples can produce appreciable scatter in elastic properties, even when porosity levels are relatively low.

In addition, large variability in Young's modulus between builds and machines has been reported. Obeidi et al. produced 316L tensile specimens on four different LPBF machines using the same powder batch and identical nominal processing parameters, yet measured elastic moduli ranging from 52 to 214 GPa across the tested conditions [37].This wide range demonstrates that machine-to-machine variability and subtle process differences can lead to very large spreads in measured modulus for PBF-LB/M 316L. Taken together, these studies show that Young's modulus in PBF-LB/M 316L is particularly sensitive to the local porosity sampled by the test, the overall defect population in each specimen, and machine and process variability [37–39]. Therefore, the relatively high standard deviation of the modulus observed in the present work is in line with the behavior reported in the literature for this material system.

Figure 6 presents the typical stress–strain curves of the samples obtained with the parameter combinations that generated the most promising results. The difference between these results is in the order of 6%, while the variability among samples of each condition was in the order of 1%, noticeably lower than that of the other parameter configurations.

As shown in Fig. 6, all specimens exhibit behavior closely resembling that of bulk AISI 316L [31]. Notably, specimen 12—produced with an increased hatching distance and reduced printing speed—demonstrates a higher Young's modulus. Similarly, specimen 9, characterized by reduced hatching and increased printing speed, displays a higher yield strength.

Figure 7 shows that higher values of the laser frequency are associated with increased ultimate tensile strength (UTS) and Young's modulus. Just looking at the energy density calculated with Eq. 1, it seems that this parameter does not influence the melting process. However, given the results presented in Table 5 of this study, we can infer that the duration of the pulses, proportional to the frequency, affects the time-dependent behavior of the melt pool.

Figure 7a–d display the mechanical properties reported in Table 5, normalized against the expected bulk values for AISI 316L. Each plot has been organized to highlight the influence of different combinations of process parameters. Due to the interdependence among parameters, two variables are represented on the horizontal axes in each diagram, while the third is implicitly dependent.

Among the measured properties, Young's modulus shows the highest variability, indicating a strong sensitivity to the process conditions applied in this study. In contrast, yield strength and ultimate tensile strength (UTS) show more consistent values across samples. The parameter combinations that resulted in the best results are highlighted in each panel.

In Fig. 7a, higher laser power combined with increased hatch distance is associated with a notable improvement in

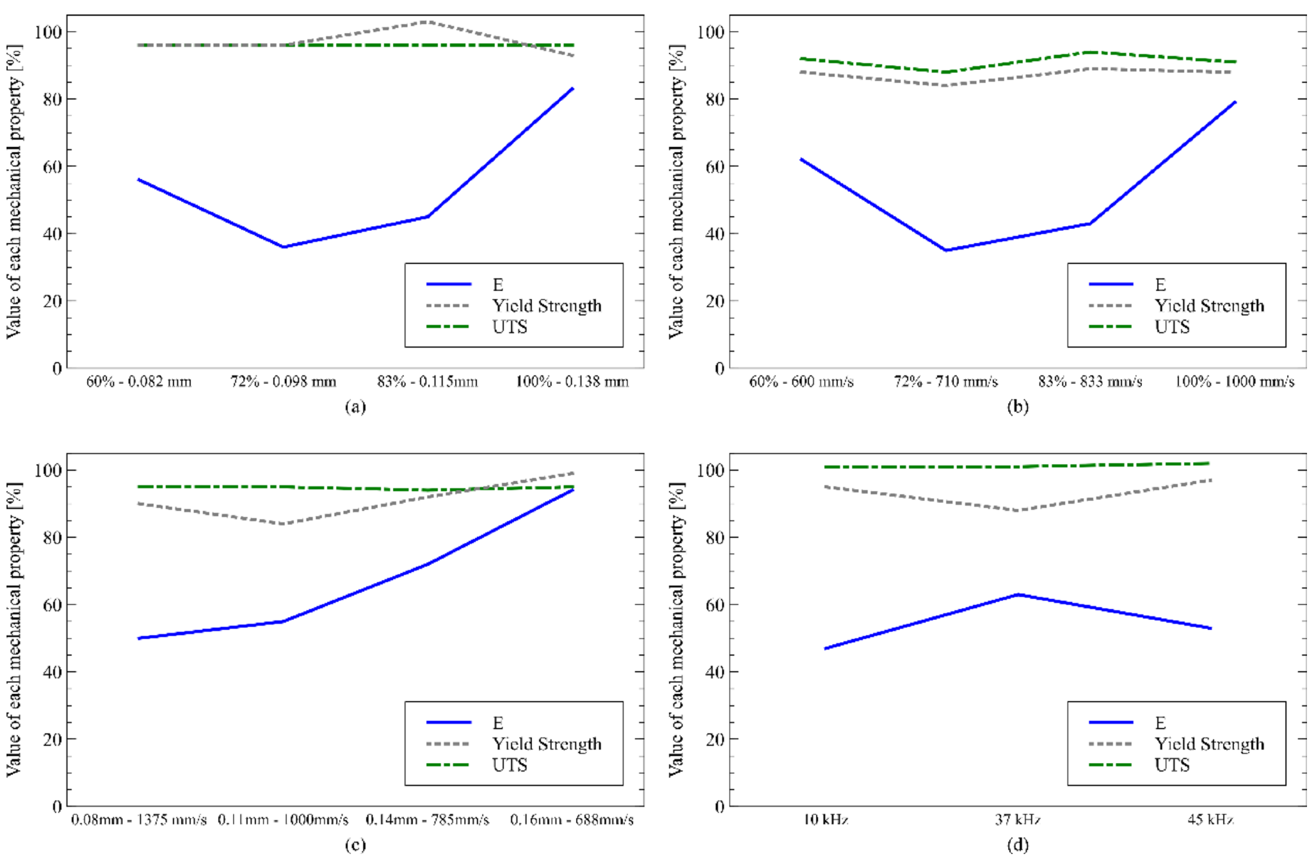

Fig. 7 **a** Influence in the mechanical properties of Laser Power and hatching distance **b** Influence in the mechanical properties of Laser Power and speed **c** Influence in the mechanical properties of hatching distance and Laser speed **d** Influence in the mechanical properties of frequency

elastic modulus. This trend is reinforced in Fig. 7b, where scan speed was varied to preserve constant energy density, confirming the positive effect of laser power. Figure 7c emphasizes the beneficial influence of a larger hatch distance on mechanical behavior.

The effect of laser frequency, in Fig. 7d, appears less pronounced. However, the data suggests that a slightly higher frequency than the default 37 kHz may offer a better trade-off between energy delivery and material response. It is known from empirical practice that the thermal output of the laser diode tends to increase at higher frequencies, although excessive frequency settings may lead to inefficiencies or instabilities and should be avoided unless specifically required.

3.2 Metallography analysis

The metallographic analysis was performed on one specimen from each of the parameter combinations listed in Table 3. The specimens were cut, polished, and etched using an Aqua Regia solution to reveal the microstructure, enabling qualitative comparison across conditions.

As expected, all specimens exhibit the characteristic microstructure of the bulk 316L austenitic stainless steel [15]. Specimen 10 was chosen as the better result and is shown in Fig. 8. Austenite and ferrite phases can be clearly identified, along with grain boundaries and columnar dendritic microstructure. Grain morphology strongly depends on the cooling rate during solidification, which, in turn, is affected by laser process parameters. Higher cooling rates result in finer grains and improved tensile strength, while slower, lower cooling rates promote coarser grains and greater ductility [16, 40].

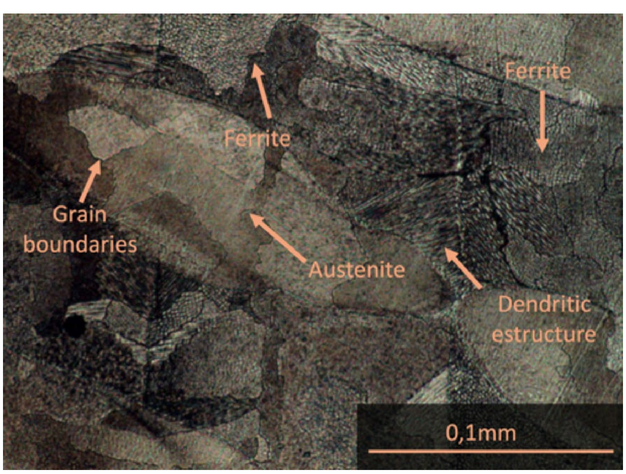

Fig. 8 Optical micrograph of specimen 10 after etching with Aqua Regia. The image reveals typical features of AISI 316L, including austenite and ferrite phases, grain boundaries, and columnar dendritic structures. The surface is parallel to the XY printing plane

The microstructure of specimens 7 and 12 which were selected for comparative analysis are shown in Fig. 9. Specimen 7 (Fig. 9a, b) manufactured with lower laser power, exhibits relatively smaller grains and defined melt track boundaries. In contrast, specimen 12 (Fig. 9c, d) produced with a value of laser power of 80%, presents larger grains and less pronounced melt lines. In several spots of specimen 12, the microstructure appears to cross the melt boundaries, suggesting diffusion phenomena during the solidification process.

The metallographic analysis of Samples 7 and 12, here presented as a more evident comparison, suggests that lower energy input can negatively affect the material's crystallization, resulting in slightly lower mechanical properties, as reported for specimen 7 in Table 5.

Weld tracks are clearly identifiable when the specimen is polished and etched on a cross-section parallel to the build plane. Although hatch distance is a nominal design parameter, the actual width of the weld tracks shows noticeable irregularity and partial overlap. This indicates that the hatch distance alone does not directly define the final melt track geometry. Instead, melt pool dynamics play a central role in determining effective weld width and track continuity.

Figure 10 presents two optical micrographs of the same sample etched along two orthogonal planes: (a) a plane parallel to the build plane and (b) perpendicular to it. The microstructure does not present evident impurities, inclusions or pores. However, the presence of distinct melt tracks in both orientations can suggest slight oxygen contamination during processing. Although the chamber was purged with argon, residual oxygen levels could have influenced local oxidation or solidification behavior at the melt pool boundaries.

3.3 Density and porosity

Density and porosity measurements were performed on one representative specimen per processing condition. The average density across all samples was 7.78 g/cm^3, which is close to the nominal bulk density of AISI 316L (7.98 g/cm^3). The total porosity varied between 0.3 and 6.9%, with open porosity representing a substantial portion in most cases. A detailed breakdown of the measured density and porosity levels is provided in Table 6.

The correlation analysis revealed a moderate-to-strong positive relationship between density and ultimate tensile strength (Pearson's r = 0.69), confirming that denser specimens tend to exhibit higher mechanical performance. This effect is consistent with the idea that enhanced layer bonding and reduced internal defects improve load transfer capabilities. In contrast, Young's modulus showed no significant correlation with porosity or density, suggesting a greater

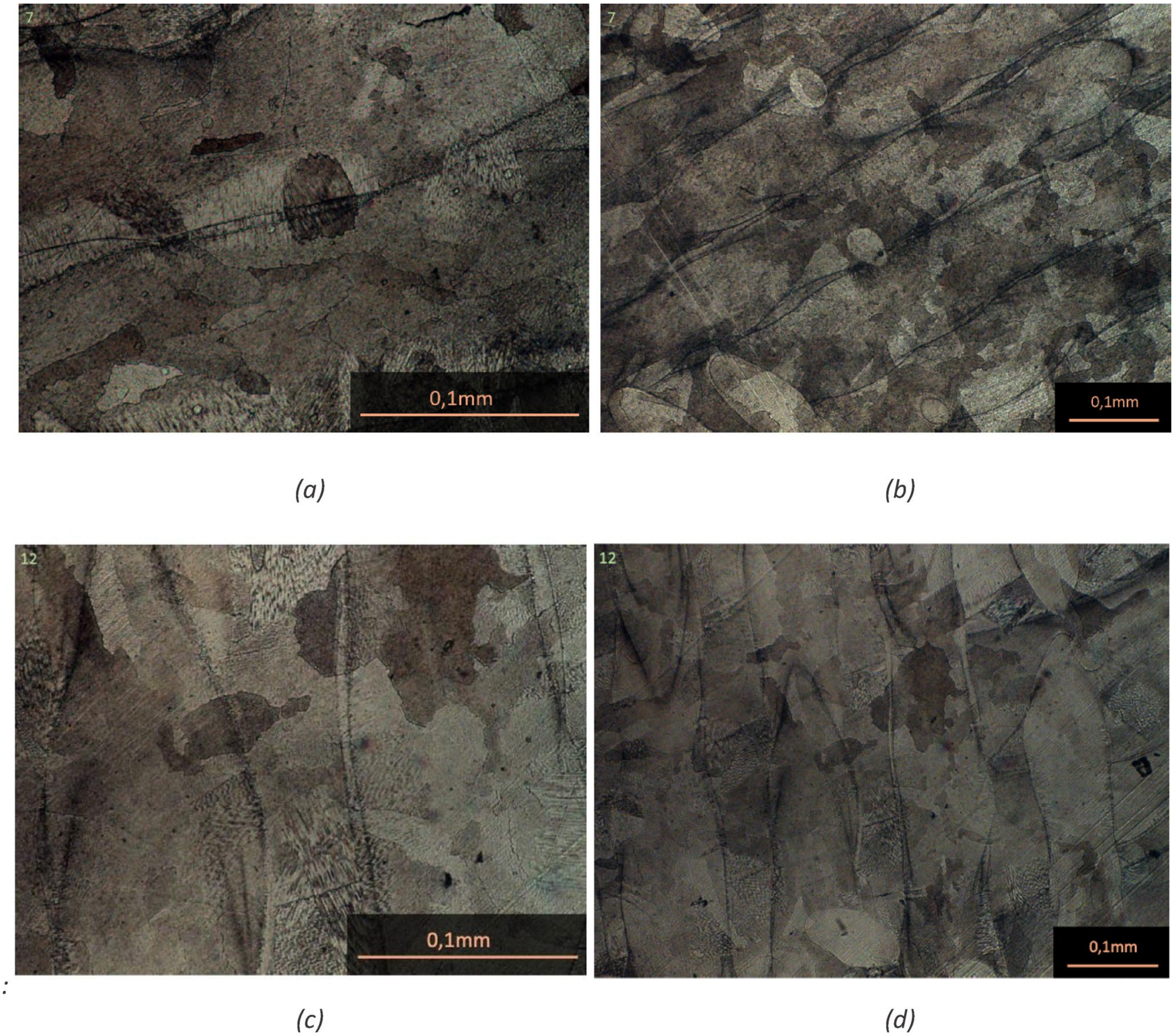

Fig. 9 **a**, **b** Microscope images of test 7–×50 (**a**) and ×20 (**b**) magnification- **c**, **d** Microscope image of test 12–×50 (**c**) and ×20 (**d**) magnification. The surfaces are parallel to the XY printing plane

sensitivity to microstructural features or anisotropy rather than bulk cohesion.

Additionally, the laser power displayed a moderate negative correlation with closed porosity (r=–0.63), indicating that higher energy input helps achieve deeper melt pools and better consolidation, thus reducing entrapped voids. These results support the use of densification metrics as predictors of mechanical integrity in PBF-LB/M-processed 316L components.

As shown in Table 6 and Fig. 11, a direct comparison of process conditions 10.1 and 10.2 isolates laser pulse frequency as the only varying parameter (lower (≈10 kHz) in 10.1 and higher (≈45 kHz) in 10.2). Despite identical power, hatch, and scan speed settings, 10.2 exhibits a noticeably higher porosity, particularly open porosity, than 10.1.

The increased laser pulse frequency can lead to keyhole instability, characterized by rapid fluctuations in melt-pool dynamics (on the order of tens of kHz) that promote pore formation through bubble trapping and collapse [41] Additionally, higher frequency may reduce time between pulses, impeding metal vapor condensation and reducing opportunity for pore escape. This is consistent with in-situ X-ray observations, which show deep keyhole regimes at higher modulation frequencies where melt-depth fluctuations are rapid and entrapped gas pockets form before the keyhole collapses [42].

Fig. 10 Etched cross-sections of specimen 9 observed under optical microscopy: **a** parallel and **b** perpendicular to the XY build plane. Melt track boundaries are clearly visible in both orientations, with no observable porosity or inclusions

Table 6 Process parameters and density/porosity average metrics for each condition

Cond	Density (g/cm^3)	Open Por. (%)	Close Por. (%)	Total Por. (%)	Power (%)	Hatch dist. (mm)	Speed (mm/s)	Frec. (kHz)	UTS (MPa)	Yield strength (MPa)
1	7.889	1.0	1.1	2.2	83	0.115	800	37	574.7	482.4
2	7.668	0.9	3.9	4.8	72	0.098	800	37	574.8	454.2
3	7.554	1.1	5.3	6.4	60	0.080	800	37	574.5	453.5
4	7.655	0.9	4.1	5.0	100	0.138	800	37	588.9	455.5
5	7.743	1.4	3.0	4.3	83	0.110	833	37	597.5	438.7
6	7.785	1.1	2.4	3.6	72	0.110	717	37	559.4	411.1
7	7.752	1.7	2.9	4.6	60	0.110	600	37	582.3	431.1
8	7.921	0.5	0.7	1.2	100	0.110	1000	37	578.8	432.4
9	7.701	1.1	3.5	4.6	80	0.080	1375	37	605.2	443.0
10	7.960	0.0	0.3	0.3	80	0.110	1000	37	603.9	413.5
11	7.754	0.6	2.8	3.5	80	0.140	785	37	598.2	454.8
12	7.898	2.8	1.0	3.8	80	0.160	688	37	604.9	485.8
1.1	7.869	1.2	1.4	2.6	83	0.115	800	10	574.9	411.2
1.2	7.937	1.1	0.5	1.7	83	0.115	800	45	574.2	383.5
5.1	7.833	1.4	1.8	3.2	83	0.110	833	10	576.3	461.6
5.2	7.817	1.2	2.0	3.2	83	0.110	833	45	575.9	406.7
10.1	7.879	0.2	1.3	1.4	80	0.110	1000	10	606.5	448.2
10.2	7.337	0.0	8.1	8.1	80	0.110	1000	45	609.0	457.4

Figure 12 depicts the porosity levels of samples 8 and 3. As shown, sample 3 exhibits a higher degree of porosity. In neither case was a lack of fusion observed.

3.4 Normalized keyhole number based on energetic balance

The traditional Keyhole Number (KH) is often used as a semi-empirical parameter to assess the transition from conduction-mode to keyhole-mode melting in PBF-LB/M processes. However, its classical formulation does not fully capture the underlying energetic requirements of the melting process, particularly when applied to pulsed laser systems. In this study, we propose a normalized version of the Keyhole Number derived from a physically grounded energy balance, comparing the effective energy input to the energy required to heat and melt a control volume of material. This approach yields a KH parameter that reflects energy input per unit time and area, which more accurately reflects the

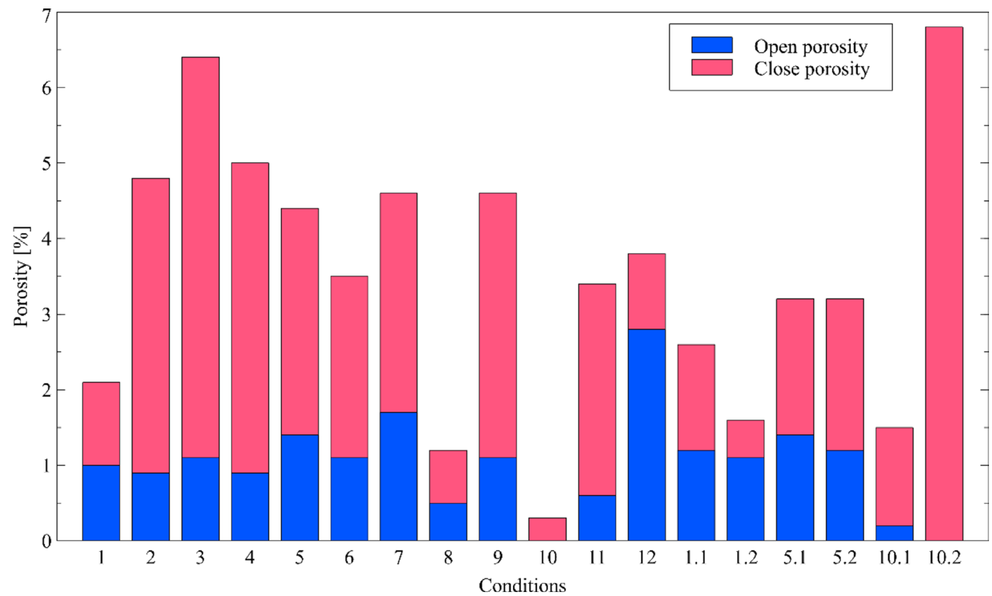

Fig. 11 Open and closed porosity (in %) for each process condition (Sample ID), shown as a stacked bar chart. Closed porosity (orange) and open porosity (blue)—representing unhealable and healable pores, respectively—reveal the contribution of each defect type to the total internal void fraction in PBF-LB/M-fabricated AISI 316L

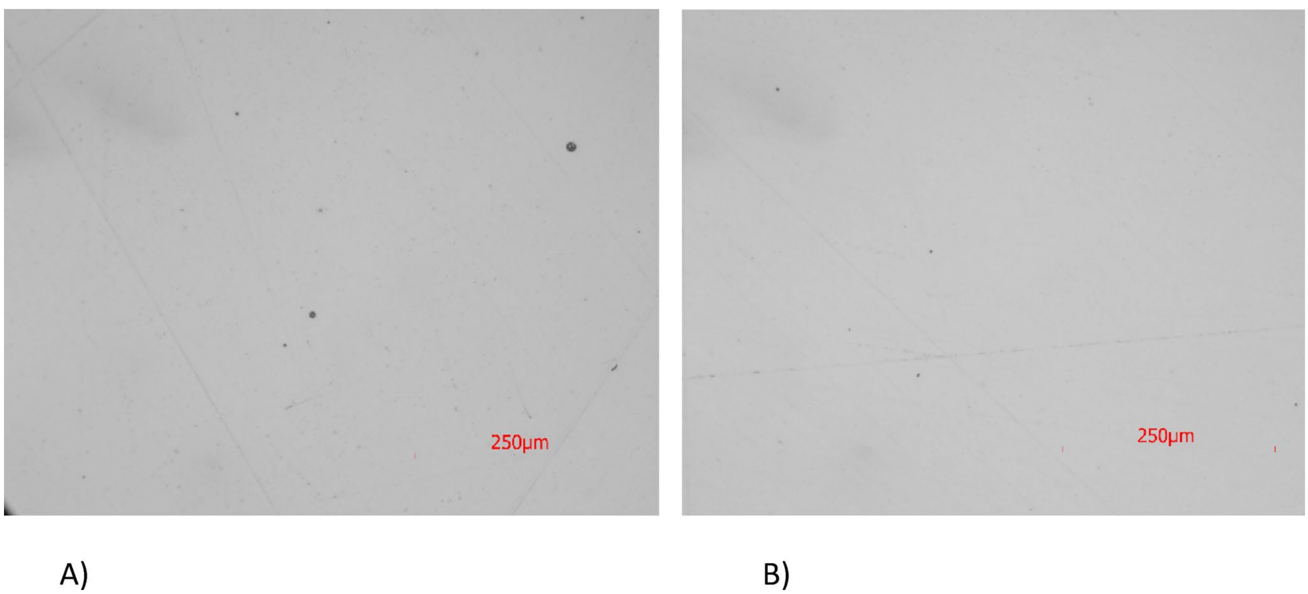

Fig. 12 Microscope images (×20 magnification) showing the porosity of **a** specimen 3 and **b** specimen 8. The surfaces are parallel to the XY printing plane

thermal dynamics of the melt pool, especially under varying laser pulse frequencies.

The normalized Keyhole Number proposed here is based on a volumetric energy balance per unit time. The effective energy supplied by the laser per second is given by:

$$E_{input} = \frac{\alpha \cdot P}{v \cdot d}$$

where α is the absorptivity of the material at the laser wavelength (≈ 0.62 for AISI 316L at 1080 nm [43]), P is the laser power (W), v is the scanning speed (mm/s), d is the hatch distance (mm).

This expression yields the effective energy density deposited per unit area and time (J/mm^2·s), assuming uniform distribution and constant laser-material interaction.

The energy required to heat and melt a unit volume of material per second can be estimated by:

$$E_{required} = \rho \cdot (C_p \cdot (T_m - T_0) + L_f) \cdot v \cdot d \cdot h$$

where ρ is the material density (g/mm^3), C_p is the specific heat capacity (J/g·K), T_m and T_0 are the melting and ambient temperatures, respectively (K), L_f is the latent heat of fusion (J/g), h is the estimated depth of energy penetration (mm), assumed constant across all samples.

Dividing E_{input} by $E_{required}$ yields a normalized Keyhole Number per second:

$$KH_{norm} = \frac{\alpha \cdot P}{\rho \cdot (C_p \cdot (T_m - T_0) + L_f) \cdot v^2 \cdot d^2 \cdot h}$$

This parameter, with units of s^{-1}, reflects the degree of excess energy per unit volume and time available to induce melt pool instability. A higher KH_{norm} value indicates a more energetic regime and is hypothesized to correlate with the formation of keyhole porosity.

This formulation compares the energy effectively deposited by the laser per unit surface and time with the energy theoretically required to heat and melt a fixed volume of material. The numerator accounts for the real energy input, adjusted by the material's absorptivity and distributed across the scan area and speed. The denominator represents the thermal demand of the material, including both sensible heat (temperature increase) and latent heat (phase change), scaled to the interaction volume. The resulting normalized Keyhole Number therefore captures how energetically aggressive the process is, with respect to the physical requirements of melting. Higher values suggest an energy surplus that can lead to deeper melt pools and potential instability, whereas values closer to unity indicate a better balance between input and demand.

3.4.1 Normalized keyhole number and total porosity

The total density vs KH_{norm} is shown in Fig. 13.

It can be seen that around KH_norm = 150, a dispersion of porosity values is observed, suggesting that other uncontrolled or unmeasured factors (e.g., laser frequency, local atmosphere, powder morphology) may influence melt pool stability near the energetic threshold.

Since the laser used in this study is a pulsed fiber laser originally designed for metal marking, the energy transfer occurs in discrete bursts at a defined pulse frequency. This frequency determines the number of energy deposition events per second. For a given average power and scanning parameters, increasing the pulse frequency reduces the energy per pulse, which in turn influences the melt pool's thermal history and stability.

To account for the pulsed nature of the laser system, we propose adjusting the normalized Keyhole Number by multiplying it by the pulse frequency f. While KH_{norm} reflects the energy balance per pulse, the product

$$KH' = KH_{norm} \cdot f$$

where f is the laser pulse frequency in kHz (pulses per second), represents the cumulative energetic excess per second. This formulation captures the effect of pulse frequency on melt pool behavior: higher values of KH′ imply a greater number of energy-rich pulses per unit time, which may lead to melt pool instability and increased porosity. Figure 14 shows the KH' vs total.

3.4.2 Normalized keyhole number based and ultimate tensile strength

In addition to its correlation with porosity, the normalized Keyhole Number also shows a moderate inverse correlation with the ultimate tensile strength (UTS) of the printed specimens, as shown in Fig. 14. Higher values of KH_{norm}—indicating increased energy input relative to the melting requirement—are associated with decreased UTS.

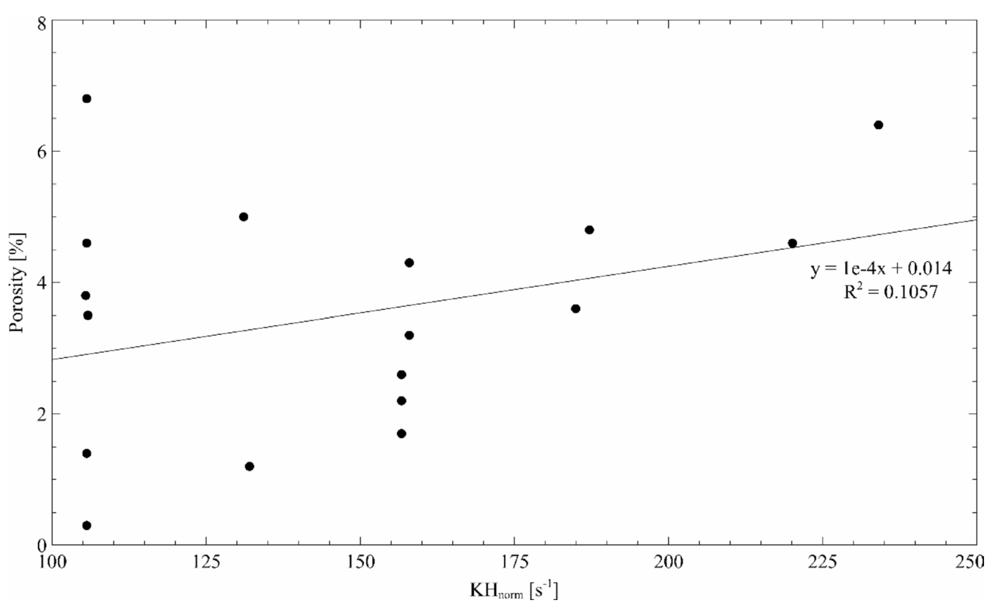

Fig. 13 Total porosity as a function of the normalized Keyhole Number (KH_norm). A minimum threshold is observed around KH_norm ≈ 150, below which porosity is generally low. However, above this value, a wide dispersion of porosity suggests that other factors beyond energy balance—such as laser frequency or powder morphology—play a significant role in keyhole formation

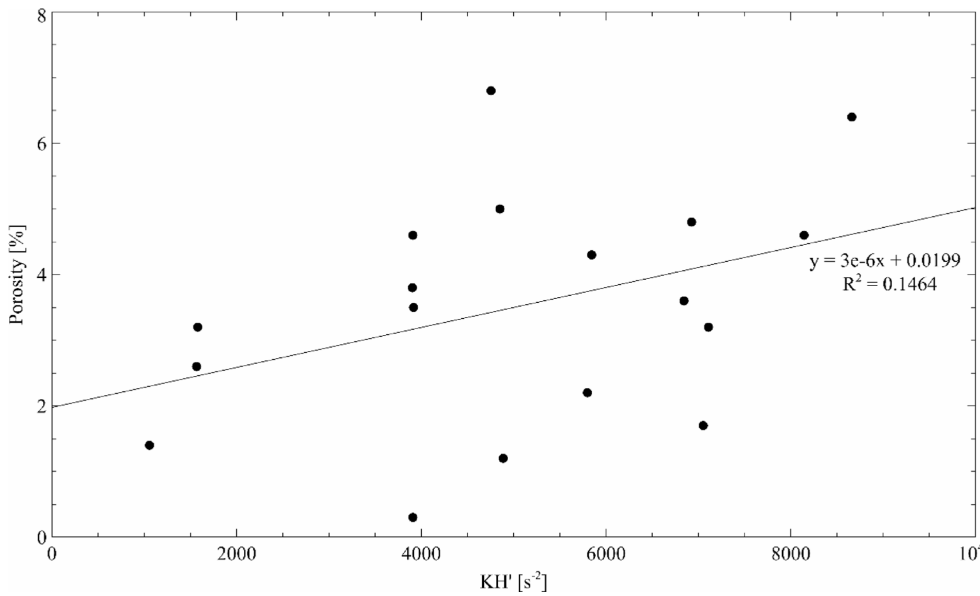

Fig. 14 Total porosity as a function of the frequency-adjusted normalized Keyhole Number (KH′). Compared to KH_{norm}, the inclusion of laser pulse frequency provides a slightly improved correlation, reinforcing the importance of pulsed energy dynamics in determining melt pool stability and porosity generation

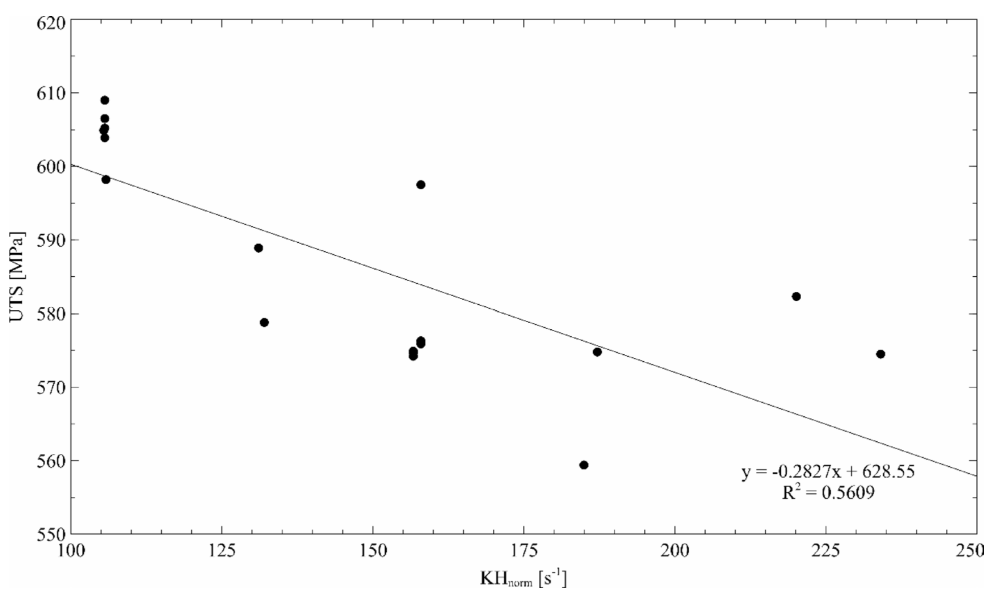

Fig. 15 Ultimate tensile strength (UTS) as a function of the normalized Keyhole Number (KH_norm). A moderate inverse correlation is observed, suggesting that higher energy input relative to the melting requirement may lead to microstructural defects and reduced mechanical performance

This trend suggests that excessive energy may contribute to the formation of microstructural defects such as sub-surface porosity, local inhomogeneities, or melt pool instability, which ultimately degrade the mechanical performance. These results support the hypothesis that melt pool energy balance plays a critical role not only in part integrity, but also in mechanical behavior (Fig. 15).

4 Conclusions

A set of specimens was manufactured using the Samylabs Alba 300 PBF-LB/M system and AISI 316L austenitic stainless-steel powder. The system employs a 300 W continuous-wave fiber laser with a 70 µm spot size, using pulse-width modulation (PWM) to reduce the power input to the material. Process parameters were varied around the values recommended by the powder manufacturer, while maintaining a constant total energy density. This work compares the effect of these parameter combinations on the resulting mechanical properties and microstructure. Although the process windows explored were narrow and specific to the material and machine, the methodology can be extended to other systems and different conditions.

The results demonstrate that increasing laser power, in combination with increased hatch distance and reduced scanning speed, led to improved mechanical performance—particularly in yield strength and ultimate tensile strength—while maintaining low porosity levels. Based on these findings and experimental feedback, the optimal parameters

Table 7 Optimal printing parameters

Parameter	Value
Frequency—F (kHz)	41
Power—P (%)	85
Power—P (W)	255
Hatch distance—DL (mm)	0,16
Laser speed—V (mm/s)	680
Layer height—Hc (mm)	0.05

deviate from the manufacturer's defaults. Specifically, an 85% laser power (255 W), a scan speed of 680 mm/s, and a hatch distance of 0.16 mm were found to provide the best balance of properties.

Importantly, the role of laser frequency—typically not considered a user-controlled parameter—was also found to influence part quality. A slightly elevated frequency (41 kHz) produced better results compared to the default setting, likely due to improved thermal input per unit time while maintaining melt pool stability. Furthermore, evaluating the influence of each processing parameter under a constant volumetric energy density provides a clearer understanding of their individual contributions to melt-pool stability, defect formation, and mechanical performance. This controlled framework strengthens the physical interpretation of the results and offers a transferable methodology that may support the optimisation of PBF-LB/M processes across different machines and materials.

A novel normalized Keyhole Number was derived to better represent the energetic conditions under pulsed laser operation. This new parameter incorporates both material thermal properties and process dynamics, including laser absorptivity and scanning strategy. When corrected by pulse frequency, the adjusted Keyhole Number (KH′) showed a stronger correlation with total porosity than traditional formulations, suggesting its potential as a predictive tool for assessing melt pool behavior and porosity formation in PBF-LB/M processes using pulse-modulated, continuous wave lasers (PWM).

Additionally, a moderate inverse correlation was observed between KH_{norm} and ultimate tensile strength, suggesting that excessive energy input may not only promote porosity but also compromise the mechanical performance of the printed parts.

The optimal PBF-LB/M parameters determined in this study for producing A316L parts with improved mechanical properties on the Samylabs Alba 300 are summarized in Table 7.

Author contributions B.A., B.C., L.P. and R.B. contributed to the conceptualization, methodology, experimental work, and writing of the main manuscript text. D.G. prepared the figures. A.L. contributed to the methodology and manuscript editing. All authors reviewed and approved the final manuscript.

Funding Open Access funding provided thanks to the CRUE-CSIC agreement with Springer Nature. This study received financial support from the Basque Government through the Research Group program IT1507-22.

Data availability No datasets were generated or analysed during the current study.

Declarations

Competing interests The authors declare no competing interests.

References

1. Yang L, Hsu K, Baughman B, Godfrey D, Medina F, Menon M, et al. Additive Manufacturing of Metals: The Technology, Materials, Design and Production Springer Series in Advanced Manufacturing. n.d
2. Kumar A, Chhabra D (2022) Adopting additive manufacturing as a cleaner fabrication framework for topologically optimized orthotic devices: Implications over sustainable rehabilitation. Clean Eng Technol 10:100559. https://doi.org/10.1016/j.clet.2022.100559
3. Springer H, Baron C, Mostaghimi F, Poveleit J, Mädler L, Uhlenwinkel V (2020) Additive manufacturing of high modulus steels: New possibilities for lightweight design. Addit Manuf 32:101033. https://doi.org/10.1016/j.addma.2019.101033
4. Spears TG, Gold SA (2016) In-process sensing in selective laser melting (SLM) additive manufacturing. Integr Mater Manuf Innov 5:16–40. https://doi.org/10.1186/s40192-016-0045-4
5. Childs THG, Hauser G, Badrossamay M (2005) Selective laser sintering (melting) of stainless and tool steel powders: Experiments and modelling. Proc Inst Mech Eng Part B J Eng Manuf 219:339–357. https://doi.org/10.1243/095440505X8109
6. Cuesta II, Díaz A, Rojo MA, Peral LB, Martínez J, Alegre JM (2022) Parameter optimisation in selective laser melting on C300 steel. Appl Sci 12:199786. https://doi.org/10.3390/app12199786
7. Praneeth J, Venkatesh S, Krishn LS (2023) Process parameters influence on mechanical properties of AlSi10Mg by SLM. Mater Today Proc. https://doi.org/10.1016/j.matpr.2022.12.222
8. Ley M, Leal B, Garza C, Reyes BB, Zambrano Robledo PDC, López Botello OE (2019) Análisis estadístico de parámetros de fabricación en AlSi10Mg mediante Manufactura Aditiva de metales 6
9. Olakanmi EO, Cochrane RF, Dalgarno KW (2015) A review on selective laser sintering/melting (SLS/SLM) of aluminium alloy powders: processing, microstructure, and properties. Prog Mater Sci 74:401–477. https://doi.org/10.1016/j.pmatsci.2015.03.002

10. Huang Z, Antion C, Toussaint F (2025) Identification for elastoplastic constitutive parameters of 316L stainless steel lattice structures using finite element model updating and integrated digital image correlation. Mech Mater 202:105232. https://doi.org/10.1016/j.mechmat.2024.105232
11. Kusoglu IM, Gökce B, Barcikowski S (2020) Research trends in laser powder bed fusion of Al alloys within the last decade. Addit Manuf 36:101489. https://doi.org/10.1016/j.addma.2020.101489
12. Pelegatti M, Benasciutti D, De Bona F, Salvati E (2023) Experimental characterization and modelling of cyclic elastoplastic response of an AISI 316L steel lattice structure produced by laser-powder bed fusion. Procedia Struct Integr 47:238–246. https://doi.org/10.1016/j.prostr.2023.07.101
13. Tridello A, Fiocchi J, Biffi CA, Chiandussi G, Rossetto M, Tuissi A et al (2020) Effect of microstructure, residual stresses and building orientation on the fatigue response up to 109 cycles of an SLM AlSi10Mg alloy. Int J Fatigue 137:105659. https://doi.org/10.1016/j.ijfatigue.2020.105659
14. Liu ZH, Zhang DQ, Sing SL, Chua CK, Loh LE (2014) Interfacial characterization of SLM parts in multi-material processing: metallurgical diffusion between 316L stainless steel and C18400 copper alloy. Mater Charact 94:116–125. https://doi.org/10.1016/j.matchar.2014.05.001
15. Rowenhorst DJ, Nguyen L, Murphy-Leonard AD, Fonda RW (2020) Characterization of microstructure in additively manufactured 316l using automated serial sectioning. Curr Opin Solid State Mater Sci. https://doi.org/10.1016/j.cossms.2020.100819
16. Saboori A, Aversa A, Marchese G, Biamino S, Lombardi M, Fino P (2020) Microstructure and mechanical properties of AISI 316L produced by directed energy deposition-based additive manufacturing: A review. Appl Sci. https://doi.org/10.3390/app10093310
17. Arısoy YM, Criales LE, Özel T, Lane B, Moylan S, Donmez A (2017) Influence of scan strategy and process parameters on microstructure and its optimization in additively manufactured nickel alloy 625 via laser powder bed fusion. Int J Adv Manuf Technol 90:1393–1417. https://doi.org/10.1007/s00170-016-9429-z
18. Keller T, Campbell Q, Hayrikyan D, Murphy K, Fitchorova O, Lesko J et al (2025) Strength, microhardness, and microstructure analysis of 316L stainless steel manufactured via hybrid laser wire and laser powder bed additive. J Manuf Process 150:1–9. https://doi.org/10.1016/j.jmapro.2025.06.037
19. Jaskari M, Hamada A, Allam T, Dzieciol K, Ghosh S, Schwaiger R et al (2025) Effects of volumetric energy density on defect structure and fatigue behaviour of powder bed fusion manufactured 316L stainless steel. Mater Sci Eng, A. https://doi.org/10.1016/j.msea.2025.147868
20. Sinico M, Witvrouw A, Dewulf W. Influence of the particle size distribution on surface quality of Maraging 300 parts produced by Laser Powder Bed Fusion. n.d.
21. Scipioni Bertoli U, Wolfer AJ, Matthews MJ, Delplanque JPR, Schoenung JM (2017) On the limitations of volumetric energy density as a design parameter for selective laser melting. Mater Des 113:331–340. https://doi.org/10.1016/j.matdes.2016.10.037
22. Greco S, Gutzeit K, Hotz H, Kirsch B, Aurich JC (2020) Selective laser melting (SLM) of AISI 316L—impact of laser power, layer thickness, and hatch spacing on roughness, density, and microhardness at constant input energy density. Int J Adv Manuf Technol 108:1551–1562. https://doi.org/10.1007/s00170-020-05510-8
23. Kurzynowski T, Stopyra W, Gruber K, Ziółkowski G, Kuznicka B, Chlebus E (2019) Effect of scanning and support strategies on relative density of SLM-ed H13 steel in relation to specimen size. Materials. https://doi.org/10.3390/ma12020239
24. Averyanova M, Cicala E, Bertrand P, Grevey D (2012) Experimental design approach to optimize selective laser melting of martensitic 17–4 PH powder: Part I - single laser tracks and first layer. Rapid Prototyp J 18:28–37. https://doi.org/10.1108/13552541211193476
25. Ng CC, Savalani M, Man HC (2011) Fabrication of magnesium using selective laser melting technique. Rapid Prototyp J 17:479–490. https://doi.org/10.1108/13552541111184206
26. Kruth JP, Froyen L, Van Vaerenbergh J, Mercelis P, Rombouts M, Lauwers B (2004) Selective laser melting of iron-based powder. J Mater Process Technol 149:616–622. https://doi.org/10.1016/j.jmatprotec.2003.11.051
27. Spierings AB, Levy G, Labhart L, Wegener K. Production of functional parts using SLM - Opportunities and limitations. Innovative Developments in Virtual and Physical Prototyping - Proceedings of the 5th International Conference on Advanced Research and Rapid Prototyping 2012:785–90. https://doi.org/10.1201/b11341-126.
28. Yang Z, Wang W, Chen Y, Wang S, Bian G, Lan L et al (2024) An experimental and numerical study on the evolution of pores and its effect on the tensile properties of LPBF Invar36 with different energy density. J Mater Res Technol 31:3064–3078. https://doi.org/10.1016/j.jmrt.2024.07.026
29. Ren-bo S, Jian-ying X, Dong-po H. Characteristics of Mechanical Properties and Microstructure for 316L Austenitic Stainless Steel 2011;18:53–9.
30. Manikandan P, Venkatesan K (2025) Role of volumetric energy density on surface quality and mechanical properties of selective laser melted 310 stainless steel. Results Eng. https://doi.org/10.1016/j.rineng.2025.104479
31. R N, Venkatesan K (2025) The effect of volumetric energy density on high-temperature dry sliding wear behaviour of 310 stainless steel fabricated by Selective Laser Melting process. Results Eng. https://doi.org/10.1016/j.rineng.2025.104722
32. Pawlak A, Rosienkiewicz M, Chlebus E (2017) Design of experiments approach in AZ31 powder selective laser melting process optimization. Arch Civ Mech Eng 17:9–18. https://doi.org/10.1016/j.acme.2016.07.007
33. Sun J, Yang Y, Wang D (2013) Parametric optimization of selective laser melting for forming Ti6Al4V samples by Taguchi method. Opt Laser Technol 49:118–124. https://doi.org/10.1016/j.optlastec.2012.12.002
34. Buhairi MA, Foudzi FM, Jamhari FI, Sulong AB, Radzuan NAM, Muhamad N et al (2023) Review on volumetric energy density: influence on morphology and mechanical properties of Ti6Al4V manufactured via laser powder bed fusion. Prog Addit Manuf 8:265–283. https://doi.org/10.1007/s40964-022-00328-0
35. Tonelli L, Fortunato A, Ceschini L (2020) CoCr alloy processed by Selective Laser Melting (SLM): effect of laser energy density on microstructure, surface morphology, and hardness. J Manuf Process 52:106–119. https://doi.org/10.1016/j.jmapro.2020.01.052
36. Wang D, Yang Y, Su X, Chen Y (2012) Study on energy input and its influences on single-track,multi-track, and multi-layer in SLM. Int J Adv Manuf Technol 58:1189–1199. https://doi.org/10.1007/s00170-011-3443-y
37. Ahmed Obeidi M, Uí Mhurchadha SM, Raghavendra R, Conway A, Souto C, Tormey D et al (2021) Comparison of the porosity and mechanical performance of 316L stainless steel manufactured on different laser powder bed fusion metal additive manufacturing machines. J Mater Res Technol 13:2361–2374. https://doi.org/10.1016/j.jmrt.2021.06.027
38. Jost EW, Miers JC, Robbins A, Moore DG, Saldana C (2021) Effects of spatial energy distribution-induced porosity on mechanical properties of laser powder bed fusion 316L stainless steel. Addit Manuf. https://doi.org/10.1016/j.addma.2021.101875
39. Weaver JS, Yin H, Redford J, Lou X (2025) Instrumented micro/macroindentation of porosity defects in laser powder bed fusion

316L stainless steel. J Mater Sci 60:9827–9842. https://doi.org/10.1007/s10853-025-10995-3
40. Martínez MA, Urdieres J, Botella J, Sánchez R, Parra R. Influencia del tamaño del grano en las propiedades mecánicas de los aceros inoxidables austeníticos Influence of grain size in mechanical properties of austenitic stainless steels. n.d.
41. Huang Y, Fleming TG, Clark SJ, Marussi S, Fezzaa K, Thiyagalingam J et al (2022) Keyhole fluctuation and pore formation mechanisms during laser powder bed fusion additive manufacturing. Nat Commun. https://doi.org/10.1038/s41467-022-28694-x
42. de Formanoir C, Hamidi Nasab M, Schlenger L, Van Petegem S, Masinelli G, Marone F et al (2024) Healing of keyhole porosity by means of defocused laser beam remelting: Operando observation by X-ray imaging and acoustic emission-based detection. Addit Manuf. https://doi.org/10.1016/j.addma.2023.103880
43. Indhu R, Vivek V, Loganathan S, Bharatish A, Soundarapandian S (2018) Overview of laser absorptivity measurement techniques for material processing. Lasers Manuf Mater Process 5:458–481. https://doi.org/10.1007/s40516-018-0075-1